

# 1 **Two years of satellite-based carbon dioxide emission quantification at the world's** 2 **largest coal-fired power plants**

3 Daniel H. Cusworth<sup>1,2</sup>, Andrew K. Thorpe<sup>3</sup>, Charles E. Miller<sup>3</sup>, Alana K. Ayasse<sup>1</sup>, Ralph Jiorle<sup>1</sup>,  
4 Riley M. Duren<sup>1,2,3</sup>, Ray Nassar<sup>4</sup>, Jon-Paul Mastrogiamomo<sup>5</sup>, and Robert R. Nelson<sup>3</sup>

5 <sup>1</sup>Carbon Mapper, Pasadena, CA, USA

6 <sup>2</sup>Arizona Institutes for Resilience, University of Arizona, Tucson, AZ, USA

7 <sup>3</sup>Jet Propulsion Laboratory, California Institute of Technology, Pasadena, CA, USA

8 <sup>4</sup>Environment & Climate Change Canada, Toronto, ON, Canada

9 <sup>5</sup>University of Toronto, Toronto, ON, Canada

10

11 Corresponding Author: Daniel H. Cusworth (dan@carbonmapper.org)

12

## 13 **Abstract**

14 Carbon dioxide (CO<sub>2</sub>) emissions from combustion sources are uncertain in many places  
15 across the globe. Satellites have the ability to detect and quantify emissions from large CO<sub>2</sub> point  
16 sources, including coal-fired power plants. In this study, we made observations with the PRecurso  
17 IperSpettrale della Missione Applicativa (PRISMA) satellite imaging spectrometer and the Orbiting  
18 Carbon Observatory-3 (OCO-3) instrument onboard the International Space Station at over 30 coal-  
19 fired power plants routinely between 2021-2022. CO<sub>2</sub> plumes were detected in 50% of acquired  
20 PRISMA scenes, which is consistent with the combined influence of viewing parameters on detection  
21 (solar illumination, surface reflectance) and unknown factors (like daily operational status). We  
22 compare satellite-derived emission rates to *in situ* stack emission observations and find average  
23 agreement to within 27% for PRISMA and 30% for OCO-3, though more observations are needed to  
24 robustly characterize the error. We highlight two examples of fusing PRISMA with OCO-2 and  
25 OCO-3 observations in South Africa and India. For India, we acquired PRISMA and OCO-3

26 observations on the same day and use the high spatial resolution capability of PRISMA (30 m  
27 spatial/pixel resolution) to partition relative contributions of two distinct emitting power plants to the  
28 net emission. Though an encouraging start, two years of observations from these satellites did not  
29 produce sufficient observations to estimate annual average emission rates within low (<15%)  
30 uncertainties. However, as the constellation of CO<sub>2</sub>-observing satellites is poised to significantly  
31 improve in the coming decade, this study offers an approach to leverage multiple observation  
32 platforms to better quantify and characterize uncertainty for large anthropogenic emission sources.

33

## 34 **1 Introduction**

35 Anthropogenic carbon dioxide (CO<sub>2</sub>) emissions are dominated by strong discrete point  
36 sources: power and other industrial combustion are estimated to make up 59% of global  
37 anthropogenic CO<sub>2</sub> emissions with transport, buildings, and other sources making up the remaining  
38 20%, 9%, and 12%, respectively (Crippa et al., 2022). Fossil fuel combustion is the largest  
39 contributor to warming trends globally since the pre-industrial era (IPCC, 2021). However, there  
40 remains uncertainty in the total magnitude of emissions from these sectors as bottom-up emission  
41 estimates rely on reported emission factors and activity data, which may vary in granularity and  
42 quality across countries and provinces (Hong et al., 2017; Guan et al., 2017). Accurate CO<sub>2</sub> emission  
43 quantification is important in light of the Paris Agreement, as participating countries must develop  
44 plans and report progress to reduce their country's greenhouse gas (GHG) emissions (UN, 2015).  
45 Leveraging atmospheric measurements, particularly satellite remote sensing, can help reduce  
46 uncertainty in facility-level CO<sub>2</sub> emission estimates, provided that the observations are accurate and  
47 sufficiently sample the facility in time (Hill and Nassar, 2019). Deployed systematically with robust  
48 error characterization, this system could be an anchor towards assessing and verifying anticipated

49 CO<sub>2</sub> emission reductions as part of national and global GHG emission reduction plans and  
50 agreements.

51 Several studies have shown that atmospheric sounding satellites can accurately quantify some  
52 point source CO<sub>2</sub> emissions from large individual coal-fired power plants. First, the Orbiting Carbon  
53 Observatory-2 (OCO-2; Crisp et al., 2017) is a space-based instrument that observes solar  
54 backscattered near-infrared radiance in the oxygen *A* band (758-772 nm; 0.04 nm spectral resolution),  
55 the weak CO<sub>2</sub> band (1594-1619 nm; 0.08 nm spectral resolution), and strong CO<sub>2</sub> band (2042-2082  
56 nm; 0.10 nm spectral resolution). OCO-2 views in nadir mode over land, while sun glint mode  
57 increases the signal over water giving measurements both land and water, and target mode to target  
58 specific validation or calibration sites. With its 10-km wide swath,  $\leq 1.3 \times 2.25$  km<sup>2</sup> pixel resolution,  
59 and better than 1.0 ppm precision for retrievals of the column-mean dry-air mole fraction of CO<sub>2</sub>  
60 (XCO<sub>2</sub>) (Taylor et al., 2023), OCO-2 is sensitive to single CO<sub>2</sub> point sources that emit sufficiently  
61 close to an OCO-2 orbital track and are spatially isolated from other major CO<sub>2</sub> sources. Using  
62 satellite observations from OCO-2, Nassar et al. (2017) detected strong CO<sub>2</sub> enhancements in the  
63 near vicinity of seven large coal-fired power plants and employed a Gaussian plume model emission  
64 quantification technique to estimate emission rates for these facilities. Further study expanded the set  
65 of facilities that could be quantified by OCO-2 (Nassar et al., 2021). Other studies have leveraged  
66 the nitrogen dioxide (NO<sub>2</sub>) retrieval capability and wide swath of the TROPOspheric Monitoring  
67 Instrument (TROPOMI; van Geffen et al., 2020) to attribute and corroborate strong CO<sub>2</sub> signals seen  
68 in OCO-2 observations (Hakkarainen et al., 2021; Reuter et al., 2019). The Orbiting Carbon  
69 Observatory-3 (OCO-3; Eldering et al., 2019), the flight spare of OCO-2, has been on board the  
70 International Space Station (ISS) since May 2019. Like OCO-2, it has been shown capable of  
71 quantifying CO<sub>2</sub> power plant emissions. Nassar et al. (2022) analyzed nine successful OCO-3

72 acquisitions of the Bełchatów Power Station and found the variability in satellite-based emission  
73 estimates agreed well with the variability in independently reported hourly power generation. Guo et  
74 al., (2023) estimated emissions at Chinese power plants using OCO-2/3 and found close agreement  
75 with emission inventories. OCO-3 is different than OCO-2 in that it has a two-axis Pointing Mirror  
76 Assembly (PMA) for more agile pointing, allowing it to rapidly point off-nadir and take Snapshot  
77 Area Mapping (SAM) mode observations over the course of two minutes. These SAMs are  
78 approximately 80×80 km<sup>2</sup> collections of measurements and are typically over sites of interest  
79 including cities, power plants, volcanoes, and flux towers.

80 Another class of remote sensing imaging spectrometers – sometimes also referred to as  
81 hyperspectral imagers – also have been shown capable of detecting and quantifying strong CO<sub>2</sub>  
82 signals from large point sources. Thorpe et al. (2017) flew the Next-Generation Airborne/Infrared  
83 Imaging Spectrometer (AVIRIS-NG) over a coal-fired power plant in Four Corners, New Mexico,  
84 and detected strong CO<sub>2</sub> plumes. AVIRIS-NG observes a large range of solar backscattered radiance  
85 (380-2500 nm), but at much coarser spectral resolution (5 nm), and high spatial resolution (e.g., 3 m  
86 when flown at 3 km altitude). The much finer spatial resolution of AVIRIS-NG allows for improved  
87 visualization of the origin of a CO<sub>2</sub> plume, but at the expense of fine precision for a single observed  
88 CO<sub>2</sub> column. Still, Cusworth et al. (2021) analyzed a combination of AVIRIS-NG and the identically  
89 built Global Airborne Observatory (GAO) at over 20 power plants in the U.S., quantified emission  
90 rates, and found close agreement with continuous emissions monitoring (CEMS) hourly emission  
91 observations. From space, the PRecursores IperSpettrale della Missione Applicativa (PRISMA),  
92 launched in 2019, like AVIRIS-NG and GAO is sensitive to a large range of solar backscattered  
93 radiance (400-2500 nm), albeit at coarser spectral and spatial resolution (10 nm spectral resolution;  
94 30 m spatial resolution; Loizzo et al., 2018). PRISMA is a tasked satellite instrument potentially

95 capable of hundreds of  $30 \times 30 \text{ km}^2$  observations per day, with equatorial crossing time of 10:30am,  
96 and target revisit of seven days, though true revisit depends on tasking priorities of the system.  
97 Cusworth et al. (2021) showed a few examples of CO<sub>2</sub> plumes detected and quantified with  
98 PRISMA, with quantified emissions similar in magnitude to reported CEMS emissions..

99         The capacity for satellites to be leveraged as useful tools for reducing uncertainty in the global  
100 CO<sub>2</sub> anthropogenic emission sector requires synthesis and routine observations (i.e., tasking) of a  
101 critical number of facilities. Therefore, in this study, we made observations at a subset of global coal-  
102 fired power plants routinely over the course of two years to probe detection limits, emission  
103 quantification uncertainty, and data yields. We observed these facilities with both OCO-3 and  
104 PRISMA. To our knowledge to date, this study represents the largest satellite-based facility scale  
105 investigation of direct CO<sub>2</sub> emission quantification across a diverse set of global power plants, and  
106 the first investigation to assess the capability of PRISMA to reliably detect and quantify CO<sub>2</sub> point  
107 sources. The results, though not sufficient by themselves to reduce uncertainty relative to bottom-up  
108 inventories significantly on an annual basis, show a path forward for data fusion and synthesis of  
109 observations from the growing constellation of planned CO<sub>2</sub> sensing satellites.

110

## 111 **2 Methods**

112         Table 1 lists the locations of all power plants we targeted during this study between 2021-  
113 2022 with PRISMA. OCO-3 includes a subset of these sites as well as other fossil fuel combustion  
114 sites as part of its list of possible targets. We identified coal-fired power plants to routinely target  
115 using a combination of bottom-up and top-down information. Bottom-up coal-fired power plant CO<sub>2</sub>  
116 emission estimates rely on activity data, that usually includes permitted capacity of a power plant  
117 and its operational state; and emission factors, usually estimated from the composition of the coal

118 that is combusted. Inventories, like the Global Energy Monitor (GEM), include this data for a large  
 119 set of coal-fired power plants across the globe (GEM, 2023). From the GEM database, we gathered  
 120 the top 10 largest bottom-up coal-fired power plants globally. We then gathered a list of top-down  
 121 TROPOMI NO<sub>2</sub> combustion hotspots, as inferred by Beirle et al. (2021). We included an additional  
 122 seven unique power plants using this dataset. Because the imaging scene size of PRISMA is 30 × 30  
 123 km<sup>2</sup>, some adjacent smaller power plants were imaged simultaneously along with these larger power  
 124 plants. In total, outside of the U.S., we made PRISMA observations at 27 power plants. In the U.S.,  
 125 we chose 10 power plants to routinely target using reported EPA CEMS information  
 126 (campd.epa.gov): five of the top 30 emitting power plants, and five progressively lower emitters,  
 127 chosen so that we could assess satellite detection capabilities.

128

129 Table 1. Power plants that were targeted specifically by PRISMA in this study.

| Power Plant Name | Country      | Latitude | Longitude | Number clear-sky observations | Number plume detections | Minimum quantified CO <sub>2</sub> emission (kt CO <sub>2</sub> h <sup>-1</sup> ) | Mean quantified CO <sub>2</sub> emission (kt CO <sub>2</sub> h <sup>-1</sup> ) | Maximum quantified CO <sub>2</sub> emission (kt CO <sub>2</sub> h <sup>-1</sup> ) |
|------------------|--------------|----------|-----------|-------------------------------|-------------------------|---|--|---|
| Mundra-Adani     | India        | 22.82    | 69.55     | 12                            | 7                       | 0.49±0.07   | 1.09±0.19  | 1.76±0.32   |
| Korba-Balco      | India        | 22.40    | 82.74     | 5                             | 1                       | NA*   | NA   | NA  |
| PLN Paiton Baru  | Indonesia    | -7.71    | 113.57    | 4                             | 2                       | NA  | NA   | NA  |
| Craig            | USA          | 40.46    | -107.59   | 5                             | 5                       | 0.56±0.11   | 0.69±0.16  | 0.8±0.22  |
| Cumberland       | USA          | 36.39    | -87.65    | 1                             | 0                       | NA  | NA   | NA  |
| Dry Fork         | USA          | 44.39    | -105.46   | 6                             | 3                       | 0.61±0.09   | 0.65±0.13  | 0.69±0.16   |
| H L Spurlock     | USA          | 38.70    | -83.82    | 5                             | 3                       | 1.15±0.32   | 1.26±0.39  | 1.37±0.45   |
| Ulsan Hanju (1)  | South Korea  | 35.49    | 129.33    | 1                             | 0                       | NA  | NA   | NA  |
| Hasdeo           | India        | 22.41    | 82.69     | 5                             | 0                       | NA  | NA   | NA  |
| Hekinan          | Japan        | 34.83    | 136.96    | 6                             | 4                       | 0.72±0.47   | 3.88±1.09  | 8.35±2.14   |
| Baotou-1         | China        | 40.66    | 109.66    | 5                             | 2                       | 0.19±0.07   | 0.27±0.07  | 0.35±0.07   |
| Kendal           | South Africa | -26.09   | 28.97     | 7                             | 2                       | 0.85±0.13   | 0.85±0.13  | 0.85±0.13   |
| NTPC Korba       | India        | 22.39    | 82.68     | 6                             | 1                       | 1.28±0.27   | 1.28±0.27  | 1.28±0.27   |

|                 |              |        |        |    |    |           |           |           |
|-----------------|--------------|--------|--------|----|----|-----------|-----------|-----------|
| Kriel           | South Africa | -26.25 | 29.18  | 8  | 3  | 0.74±0.15 | 0.82±0.15 | 0.95±0.16 |
| Labadie         | USA          | 38.56  | -90.84 | 4  | 4  | 0.73±0.18 | 0.73±0.18 | 0.73±0.18 |
| Martin Lake     | USA          | 32.26  | -94.57 | 8  | 8  | 1.45±0.31 | 2±0.59    | 2.6±0.98  |
| Matimba         | South Africa | -23.67 | 27.61  | 11 | 8  | 0.33±0.05 | 0.72±0.16 | 1.14±0.32 |
| Matla           | South Africa | -26.28 | 29.14  | 8  | 3  | 0.33±0.05 | 0.77±0.15 | 1.37±0.27 |
| Medupi          | South Africa | -23.71 | 27.56  | 15 | 12 | 0.33±0.06 | 0.83±0.19 | 1.47±0.34 |
| Mundra-Tata     | India        | 22.82  | 69.53  | 12 | 5  | 0.38±0.09 | 0.74±0.13 | 1.32±0.21 |
| Niederaussem    | Germany      | 51.00  | 6.67   | 1  | 0  | NA        | NA        | NA        |
| Oregon          | USA          | 41.67  | -83.44 | 5  | 1  | NA        | NA        | NA        |
| Paiton-3        | Indonesia    | -7.71  | 113.58 | 4  | 4  | 1.54±0.37 | 3.16±0.69 | 4.78±1.02 |
| Rihand          | India        | 24.03  | 82.79  | 8  | 5  | 0.83±0.17 | 0.99±0.26 | 1.36±0.38 |
| Sanfeng         | China        | 40.66  | 109.76 | 6  | 0  | NA        | NA        | NA        |
| Sasan           | India        | 23.98  | 82.63  | 9  | 7  | 0.65±0.15 | 1.01±0.24 | 1.51±0.31 |
| Sooner          | USA          | 36.45  | -97.05 | 6  | 3  | 1.05±0.22 | 1.05±0.22 | 1.05±0.22 |
| Togtoh          | China        | 40.20  | 111.36 | 2  | 2  | 0.25±0.06 | 0.91±0.17 | 1.58±0.27 |
| Ulsan Hanju (2) | South Korea  | 35.47  | 129.38 | 1  | 0  | NA        | NA        | NA        |
| Vindhyachal     | India        | 24.10  | 82.68  | 9  | 7  | 0.33±0.1  | 0.72±0.15 | 1.24±0.23 |
| Waigaoqiao      | China        | 31.36  | 121.60 | 6  | 1  | NA        | NA        | NA        |
| Yeosu Hanwha    | South Korea  | 34.84  | 127.69 | 2  | 0  | NA        | NA        | NA        |
| Yosu            | South Korea  | 34.83  | 127.67 | 2  | 0  | NA        | NA        | NA        |
| Al Zour         | Kuwait       | 28.71  | 48.37  | 12 | 0  | NA        | NA        | NA        |

130 \*A value of “NA” indicates that no plumes were detected at this power plant or that the emission quantification  
131 algorithm (described in Methods) failed to quantify an emission rate.  
132

133 *2.1 PRISMA observations and quantification*

134 PRISMA is a tasked satellite instrument, capable of collecting around 200 30 × 30 km<sup>2</sup> targets  
135 per day and has 20° pointing capability off nadir. Authenticated users can program single observation  
136 requests through PRISMA’s web portal (prisma.asi.it), which currently allows for 13 concurrent  
137 requests at a time per user. We specified two-week observing windows for each request, and  
138 configured requests to collect if the scene-averaged solar zenith angle (SZA) was less than 70° and

139 forecast meteorology anticipated less than 20% cloud cover. If the orbital configuration, weather,  
 140 SZA align and there are no other conflicting or higher priority requests, PRISMA images a target.

141 For each acquired PRISMA image, we performed XCO<sub>2</sub> retrievals on all pixels within a 2.5  
 142 km radius around the power plant. We retrieve XCO<sub>2</sub> using the Iterative Maximum A Posteriori –  
 143 Differential Optical Absorption Spectroscopy (IMAP-DOAS) algorithm, as implemented in  
 144 Cusworth et al. (2021). This approach estimates XCO<sub>2</sub> by decomposing an observed radiance  
 145 spectrum into high and low frequency features between 1900-2100 nm. For high-frequency features,  
 146 we simulate atmospheric transmission of CO<sub>2</sub>, H<sub>2</sub>O, and N<sub>2</sub>O using a Beer-Lambert approximation.  
 147 For low-frequency features (e.g., surface reflectance, aerosol scattering), we use an 8-degree  
 148 polynomial. The forward model that drives IMAP-DOAS therefore has the following form:

$$149 \quad F^h(\mathbf{x}) = I_0(\lambda) \exp \left( - \sum_{n=1}^6 s_n \sum_{l=1}^{72} A_l \tau_{n,l} \right) \sum_{k=0}^K a_k \lambda^k \quad (1)$$

150 Where  $F^h$  is simulated backscattered radiance at wavelength  $\lambda$ ,  $I_0$  is incident solar intensity,  $A_l$  is the  
 151 airmass factor at vertical level  $l \in [1,72]$ ,  $\tau_{n,l}$  is the optical depth for each trace gas element,  $s_n$  is the  
 152 scaling factor applied to the optical depth, and  $a_k$  is a polynomial coefficient ( $K=8$ ). Optical depths  
 153 are computed by querying meteorological information for pressure and temperature from the  
 154 MERRA-2 reanalysis (Gelaro et al., 2017), and using that information to select proper HITRAN  
 155 absorption cross sections for each trace gas (Kochanov et al., 2016). To compare the model from  
 156 Equation 1 against PRISMA observed radiance ( $\mathbf{y}$ ), we compute  $F^h(\mathbf{x})$  between 1900-2100 nm at  
 157 0.02 nm resolution, then convolve the output using the PRISMA full-width half maximum, and  
 158 sample at PRISMA wavelength positions. This results in vector  $\mathbf{F}(\mathbf{x})$  that is comparable to  $\mathbf{y}$ . The  
 159 vector  $\mathbf{x}$ , also called the state vector, includes scale factors for CO<sub>2</sub>, H<sub>2</sub>O, N<sub>2</sub>O, and polynomial  
 160 coefficients:  $\mathbf{x} = (s_{CO_2}, s_{H_2O}, s_{N_2O}, a_0, \dots, a_8)$ .



161 XCO<sub>2</sub> is retrieved from PRISMA radiance using a Bayesian optimal estimation approach  
 162 (Rodgers, 2000). Here, the optimized state vector solution, or posterior, is solved through Gauss-  
 163 Newton iteration:

$$164 \quad \mathbf{x}_{i+1} = \mathbf{x}_A + (\mathbf{K}_i^T \mathbf{S}_0^{-1} \mathbf{K}_i + \mathbf{S}_A^{-1})^{-1} \mathbf{K}_i^T \mathbf{S}_0^{-1} [y - \mathbf{F}(\mathbf{x}_i) + \mathbf{K}_i(\mathbf{x}_i - \mathbf{x}_A)] \quad (2)$$

165 Where  $\mathbf{S}_0 = [\boldsymbol{\epsilon}\boldsymbol{\epsilon}^T]$  is the observation error covariance matrix defined by the instrument signal to noise  
 166 ratio (SNR),  $\mathbf{x}_A$  is the prior estimate of the state vector, and  $\mathbf{S}_A$  is the prior error covariance matrix.  
 167 The matrix  $\mathbf{K}$ , or Jacobian matrix, represents the first derivative of the  $\mathbf{F}(\mathbf{x})$  with respect to the state  
 168 vector:

$$169 \quad \mathbf{K}_i = \left. \frac{\partial \mathbf{F}}{\partial \mathbf{x}} \right|_{\mathbf{x}=\mathbf{x}_i} \quad (3)$$

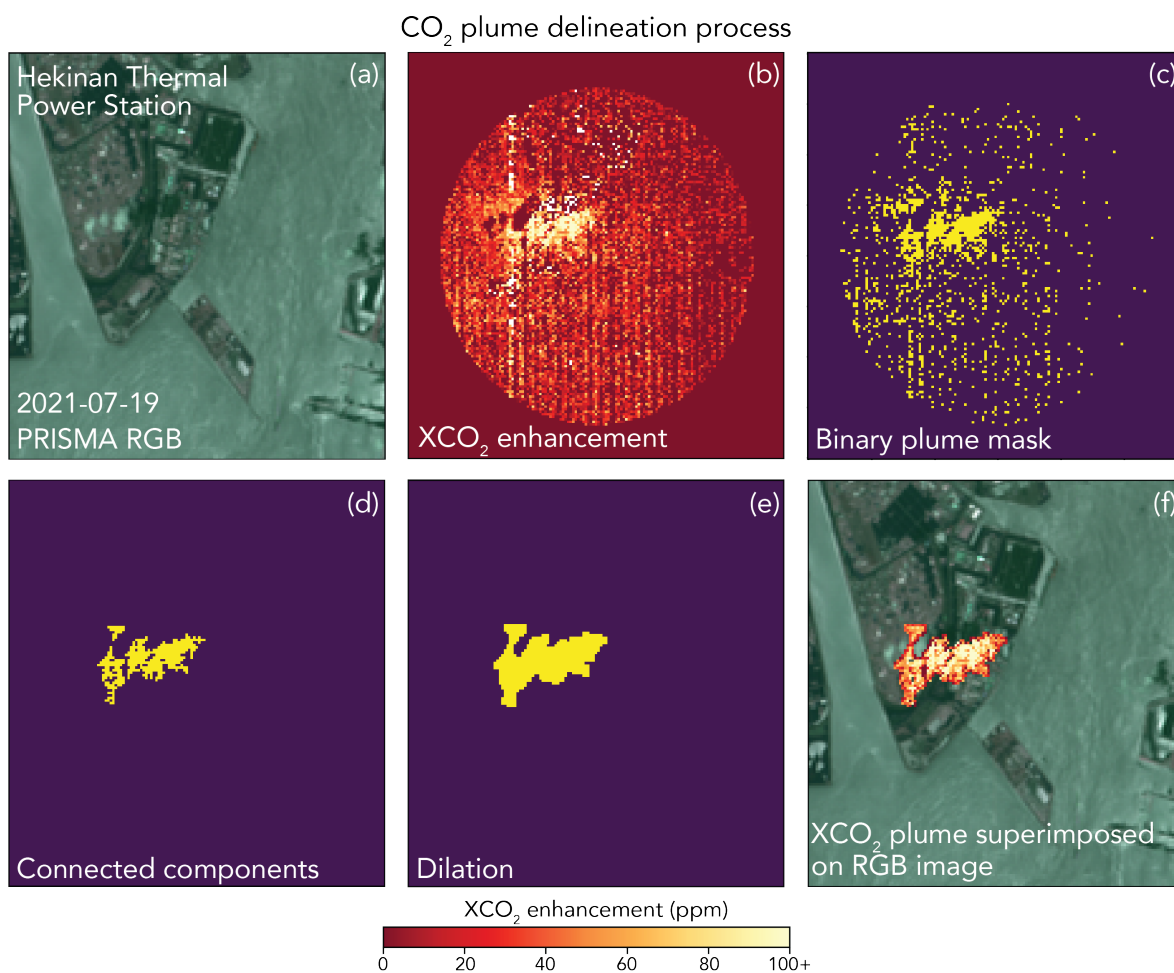
170 The posterior error covariance matrix can be computed explicitly to quantify retrieval precision:

$$171 \quad \hat{\mathbf{S}} = (\mathbf{K}_i^T \mathbf{S}_0^{-1} \mathbf{K}_i + \mathbf{S}_A^{-1})^{-1} \quad (4)$$

172 Across the scenes we acquired with PRISMA, using this retrieval approach, we quantify an  
 173 average 3.3 ppm precision for an XCO<sub>2</sub> column. Absolute biases in PRISMA XCO<sub>2</sub> retrievals are  
 174 less important for CO<sub>2</sub> plume detection and quantification: systematic retrieval biases are removed  
 175 from a scene through the quantification and removal of a local background, as described below. To  
 176 characterize bias in emission quantification, we compare emission rates derived from PRISMA to  
 177 stack-level CEMS measurements (Section 3.2).

178 We quantified emissions for each PRISMA plume detection using the Integrated Mass  
 179 Enhancement (IME) approach (Cusworth et al., 2021). However, we updated the masking scheme  
 180 for this analysis to produce more reliable masks for each CO<sub>2</sub> plume. Figure 1 shows the plume  
 181 masking procedure for a plume detected at the Hekinan, Japan power plant on July 19, 2021. First,  
 182 we apply a background threshold to differentiate candidate plume pixels from the background

183 (method to quantify background threshold described in Section 3.2). We then group enhanced XCO<sub>2</sub>  
184 pixels into clusters of at least 20 connected pixels. These groups are then buffered with a one-pixel  
185 dilation filter to smooth edges and any gaps that exist in a group (Dougherty, 1992). Finally, each  
186 cluster is considered part of the plume if at least one of its pixels is within 500 m of an exhaust stack.



187  
188 **Figure 1.** Example of the plume delineation and masking process performed on XCO<sub>2</sub> retrievals  
189 derived from PRISMA observations. Panel (a) shows the simultaneously observed RGB PRISMA  
190 imagery, panel (b) shows retrieved XCO<sub>2</sub> above the background, panels (c)-(e) show the plume  
191 masking procedure to isolate enhanced pixels and remove noise, and panel (f) shows the resulting  
192 CO<sub>2</sub> plume superimposed on the RGB imagery.

193

194 IME is calculated for a plume using the following equation:

195 
$$\text{IME} = \sum_{i=1}^N \Delta\Omega_i \Lambda_i \quad (5)$$

196 where  $\Delta\Omega_i$  is the XCO<sub>2</sub> mass enhancement in pixel  $i$  relative to background (kg m<sup>-2</sup>),  $\Lambda_i$  is the pixel  
197 area (900 m<sup>2</sup>), and  $N$  is the number of pixels in the plume. The CO<sub>2</sub> emission rate  $Q$  is estimated from  
198 the IME using the following relationship:

199 
$$Q = \frac{U_{eff}}{L} \text{IME} \quad (6)$$

200 where  $L = \sqrt{\sum_{i=1}^N \Lambda_i}$  is the plume length and  $U_{eff}$  is the effective wind speed. The parameter  $L$  is an  
201 operational parameter that needs to be related to the extent of the plume. Since a plume dissipates in  
202 all directions due to turbulent diffusion, an explicit scaling function (i.e., an effective wind speed  
203  $U_{eff}$ ) that relates  $L$  and 10 m wind speed ( $U_{10}$ ) to the true emission can be derived through large eddy  
204 simulations (Varon et al., 2018):~~The effective wind speed relates IME and plume length~~  
205 ~~parameterizations to true emission rates. This relationship can be empirically estimated through large~~  
206 ~~eddy simulations using the 10 m wind speed ( $U_{10}$ ). Here we apply the  $U_{eff}$  relationship derived from~~  
207 ~~Varon et al., 2018:~~

208 
$$U_{eff} = 1.1 \log U_{10} + 0.6. \quad (7)$$

209 where  $U_{eff}$  and  $U_{10}$  are in units of [m s<sup>-1</sup>]. We query the ERA5-Land reanalysis using the Open-Meteo  
210 Application Programming Interface (open-meteo.com), which provides hourly wind information  
211 globally at 0.1° spatial resolution (Muñoz-Sabater et al., 2021). Uncertainty due to winds is calculated  
212 by generating an ensemble of  $U_{10}$  values assuming 50% error (Cusworth et al., 2021). Uncertainty  
213 due to the CO<sub>2</sub> background is calculated by generating many emission estimates and calculating a

214 standard deviation using an ensemble of background thresholds. Background thresholds are set to  
215 vary with scene-averaged CO<sub>2</sub> retrieval precision. Total emission uncertainty is estimated by adding  
216 in quadrature the contribution of wind and background uncertainties.

217

## 218 *2.2 OCO-3 observations and quantification*

219 OCO-3 is also a tasked mission: it can take SAMs over any place of interest within the latitude  
220 range of the ISS orbit (about 52° S to 52° N). In addition to the SAM locations we supplied to OCO-  
221 3 to overlap with PRISMA targets, there are many other power plant and fossil fuel combustion  
222 sources that make up its set of mission targets. However, unlike PRISMA, OCO-3 does not consider  
223 cloud forecasts, snow cover, or viewing geometry when planning SAMs and thus the majority of  
224 observations fail to produce useful maps of XCO<sub>2</sub>. Additionally, aerosol- and albedo-induced XCO<sub>2</sub>  
225 artifacts are present in many SAMs (Bell et al., 2023) and thus make the detection of plumes even  
226 more difficult.

227 For all cloud-free soundings, OCO-3 XCO<sub>2</sub> concentrations are derived using the  
228 Atmospheric Carbon Observations from Space (ACOS; O'Dell et al., 2012; Crisp et al., 2012; O'Dell  
229 et al., 2018) v10 optimal estimation retrieval, which employs the Levenberg-Marquardt modification  
230 of the Gauss-Newton method. In this work, bias corrected XCO<sub>2</sub> from the OCO-3 Lite files is used  
231 but the official data quality flag is not applied. This was done because often the quality flag removes  
232 XCO<sub>2</sub> retrievals within the plume and makes emission estimation more difficult or impossible  
233 (Nassar et al., 2022). For SAMs where we visually identified CO<sub>2</sub> plumes (e.g., Figure 2), emission  
234 rates are estimated using two approaches: (1) a Gaussian plume model and (2) the IME method. For  
235 the Gaussian plume model approach, we follow the algorithm outlined in Nassar et al. (2022):

236 
$$V(x, y) = \frac{Q}{\sqrt{2\pi}\sigma_y(x)u} e^{-\frac{1}{2}\left(\frac{y}{\sigma_y(x)}\right)^2} \quad (8)$$

237 
$$\sigma_y(x) = a \cdot \left(\frac{x}{x_o}\right)^{0.894} \quad (9)$$

238 Where  $V$  represents the vertical columns within the plume ( $\text{g}/\text{m}^2$ ),  $Q$  is the  $\text{CO}_2$  emission rate ( $\text{g}/\text{s}$ ),  
 239  $y$  is the wind direction perpendicular to the plume (m),  $u$  is the wind speed at the height of the plume  
 240 at its midline (m/s) assuming plume rise of 250 m above the stack height,  $\sigma_y(x)$  is the standard  
 241 deviation of the  $y$ -direction,  $x_o$  is a characteristic plume length (1000 m), and  $a$  is a stability  
 242 parameter (Nassar et al., 2021). Following Nassar et al. (2022), wind speed and direction inputs are  
 243 estimated by taking the average of ERA-5 (Bell et al., 2020) and MERRA-2 reanalysis data. The  
 244 wind direction is optimized by rotating the plume, typically between  $-30^\circ$  to  $30^\circ$  away from the mean  
 245 ERA-5/MERRA-2 direction, and calculating the correlation coefficient ( $R$ ) of the modeled and  
 246 observed  $\text{XCO}_2$ . The optimized wind direction is the direction that produces the largest  $R$ . The  
 247 background is typically estimated by averaging OCO-3 footprints within a radius of 30 km, excluding  
 248 the plume itself and a narrow 3 km buffer zone. However, if there are visible artifacts in the  $\text{XCO}_2$   
 249 background that are unrelated to the power plant plume, the background field is modified to avoid  
 250 them. For example, decreasing the radius of footprints used from 30 km to 20 km. The uncertainty  
 251 in wind speed is calculated by taking the difference of the emission estimate using two different  
 252 models (ERA-5 and MERRA2). The background concentration uncertainty is calculated by  
 253 estimating  $Q$  using three different background radii of 30, 40, and 50 km.  $Q$  is also calculated for a  
 254 30 km radius background but only using the left and right halves of the background, relative to the  
 255 direction of the plume. The standard deviation of both these methods is calculated and the larger of  
 256 the two is the background uncertainty. The plume rise uncertainty is calculated by estimating  $Q$  using  
 257 plume rise values of 100, 200, 250, 300, and 400 m and taking the standard deviation of those values.

258 Total uncertainty on the emission rate  $Q$  using the Gaussian plume method is estimated by adding in  
259 quadrature the contribution of wind speed, background concentration, and plume rise uncertainties.

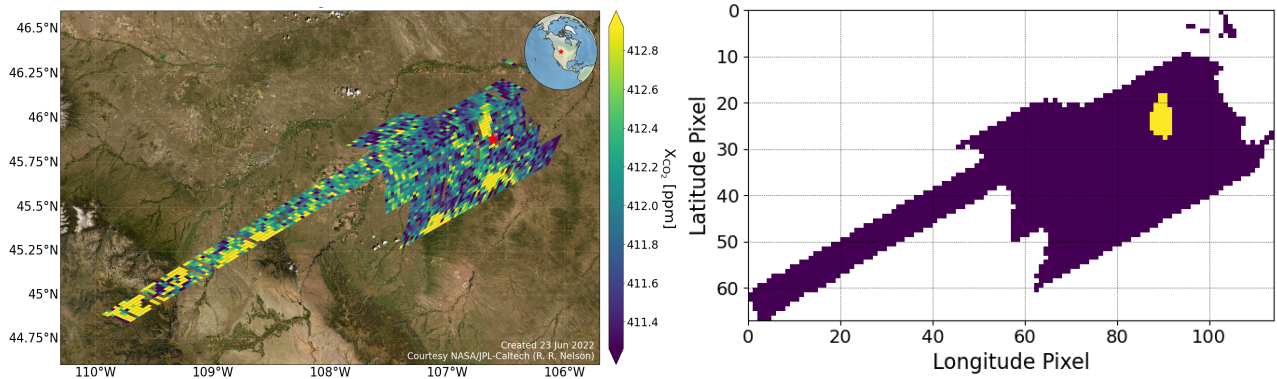
260 To obtain another estimate of emission rate, we also apply an IME quantification approach to  
261 the CO<sub>2</sub> plumes, which to our knowledge is the first time the IME method has been applied to OCO-  
262 3 SAMS at coal power plants. We first interpolate the XCO<sub>2</sub> retrievals in a SAM to a uniform  $2 \times 2$   
263 km<sup>2</sup> grid to account for occasional OCO-3 footprint overlap. Similar to Varon et al. (2018),  $3 \times 3$   
264 pixel neighborhoods are sampled and the distributions are compared to the background using a  
265 Student's  $t$ -test. The default confidence level for the  $t$  test is 95% but this is often lowered to visually  
266 capture most of the plume. The plume is then smoothed using a  $3 \times 3$  pixel median filter and a  
267 Gaussian filter with a standard deviation of 0.5. The  $U_{eff}$  calculation is done using an equation  
268 approximately equal to Equation 7 ( $U_{eff} = 1.0 \log U_{10} + 0.55$ ). Other recent studies have used various  
269 methods (Lin et al., 2023; Brunner et al., 2023), but further research is needed to determine the most  
270 accurate way to estimate  $U_{eff}$  for an OCO-3-like instrument. The wind direction is the optimized  
271 direction determined by the Gaussian plume model. The background XCO<sub>2</sub> estimate is taken from  
272 the Gaussian plume model methodology and the plume is typically required to be within 50 km  
273 downwind and 8 km crosswind of the source, although these parameters are modified if the plume  
274 curves outside of the 8 km crosswind threshold or there are XCO<sub>2</sub> artifacts that should be avoided.

275 The uncertainty for the IME method is estimated similarly to the Gaussian plume model  
276 method. The uncertainty in wind speed is calculated by taking the standard deviation of the emission  
277 estimates using wind speed from two different models (ERA-5 and MERRA2). The background  
278 concentration uncertainty is calculated by estimating  $Q$  using the different backgrounds calculated in  
279 the Gaussian plume model method: a 20 km radius, 30 km radius, 40 km radius, left half, full circle,  
280 and right half. The standard deviation of the three radii estimates and left half, full circle, and right

281 half estimates are calculated and the larger of the two is the background uncertainty. Uncertainty of  
282 the Student's  $t$ -test confidence level is also estimated. The confidence level and -10% and +10% of  
283 the confidence level are used to find  $Q$ . For example, if the confidence level needed to visually  
284 capture the XCO<sub>2</sub> plume is 85%,  $Q$  is calculated for 75%, 85%, and 95% and the standard deviation  
285 of those three values represents the confidence level uncertainty. Total uncertainty on the emission  
286 rate  $Q$  using the IME method is estimated by adding in quadrature the contribution of wind speed,  
287 background concentration, and Student's  $t$ -test confidence level uncertainties.

288 Figure 2 shows IME methodology successfully identifying an XCO<sub>2</sub> plume from an OCO-3  
289 SAM taken over the Colstrip power plant.

290



291

292 **Figure 2.** IME plume identification approach applied to an example OCO-3 SAM at the Colstrip  
293 power plant on 18 August 2021. Left panel: OCO-3 SAM bias corrected XCO<sub>2</sub>. Right panel: yellow  
294 pixels indicate the final plume mask.

295

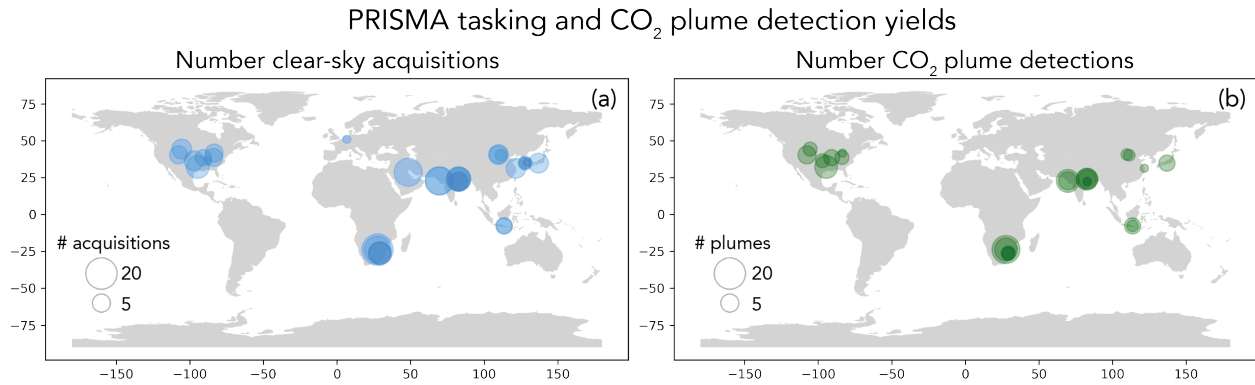
### 296 **3 Results**

297 *3.1 Global yields from two years of observations*

298 Figure 3a shows a global map of power plants we targeted with PRISMA, with the marker  
299 for each power plant's location (latitude, longitude) scaled to represent the number of successful  
300 acquisitions between 2021-2022. In total, we acquired 181 PRISMA images, which corresponds to  
301 314 unique power plant observation scenes. Of these scenes, 210 were of sufficient quality to attempt  
302 CO<sub>2</sub> retrieval and plume detection, with quality mostly determined by visual inspection for clouds  
303 and haze. Of these 210 scenes, 104 were determined to have CO<sub>2</sub> plumes (Figure 3b). Scenes were  
304 marked as containing CO<sub>2</sub> plumes through inspection of XCO<sub>2</sub> and visible imagery: if a large cluster  
305 of pixels with elevated XCO<sub>2</sub> above the background were also in the vicinity of a power plant exhaust  
306 stack, an analyst would mark the scene as containing a CO<sub>2</sub> plume. Routine tasking observations with  
307 PRISMA resulted in an average of 6 acquisitions for each power plant (maximum 15), roughly one  
308 image acquired per quarter. Of these acquisitions, plumes were detected on average four times per  
309 facility (maximum 12).

310 For OCO-3, 1363 power plant SAMs were taken during September 2019 to December 2022.  
311 Of these, 139 XCO<sub>2</sub> plumes emanating from power plants were visually identified. However, only  
312 14 were for power plants that were also observed by PRISMA and have CEMS validation (nine  
313 Colstrip cases, two Martin Lake cases, and three Craig cases). The acquisition rates are low relative  
314 to PRISMA because OCO-3 does not account for scene favorability when planning its SAMs. For  
315 example, OCO-3 took 66 Colstrip SAMs from 2019-2022 yet only yielded nine high-quality XCO<sub>2</sub>  
316 plume cases.





317

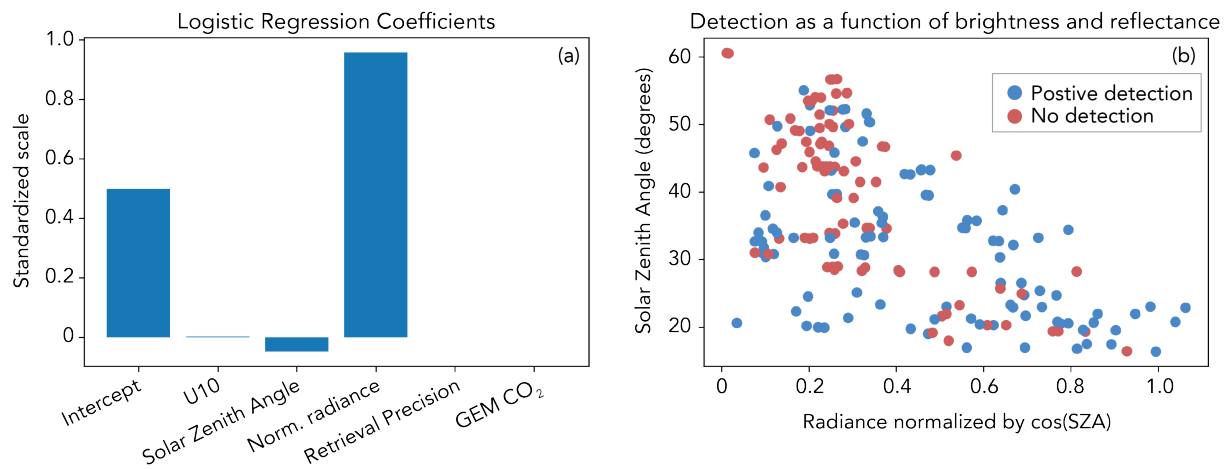
318 **Figure 3.** Data yields from PRISMA continually between 2021-2022. Panel (a) shows the number  
 319 of clear-sky acquisitions for each power plant. Panel (b) shows the number of plumes detected by an  
 320 analyst for each of the observed power plants.

321

322         The low observed average detection rate of CO<sub>2</sub> plumes is a result of three primary factors:  
 323 (1) observing conditions at each facility including solar zenith angle (SZA) and surface reflectance;  
 324 (2) local meteorology; and (3) operational status at each power plant at the time of acquisition. To  
 325 test how well these factors predict the presence of a plume for PRISMA, we fit a logistic regression  
 326 classification function with a sparse (L1) penalty to our dataset (Fan et al., 2008). This algorithm fits  
 327 a logit function to the plume detection outcome of each scenes (i.e., detected plume = TRUE, no  
 328 detected plume = FALSE) using a set of predictor variables that are likely candidates to explain  
 329 prediction results. In this setup, the statistical model is fit using the following predictor variables –  
 330 SZA,  $U_{10}$ , average single-sounding retrieval precision across the scene, annual bottom-up emission  
 331 estimate for the power plant using GEM, and average observed radiance between 1900-2100 nm  
 332 within the scene normalized by the cosine of the SZA. This last factor is a simple proxy for surface  
 333 reflectance, although it does not take into account other factors that influence radiance observations  
 334 (e.g., water vapor, aerosols, other atmospheric constituents). We split the data so that 50% was used

335 to train the model and 50% was reserved as a test set. The predictor variables were all standardized  
336 by their mean and standard deviation before the model was fit. The results of classification can be  
337 summarized using two statistics: precision (ratio of true positives to sum of true positives and false  
338 positives) and recall (ratio of true positives to sum of true positives and false negatives). The results  
339 of fitting a logistic regression model to the data show minor prediction performance, with precision  
340 = 0.60 and recall = 0.69 for positive plume detection. The regression coefficients are shown in Figure  
341 4a. The coefficient with the highest weight is normalized radiance. Figure 4b shows SZA against  
342 normalized radiance, with red dots indicating no plume detection and blue dots representing positive  
343 plume detection. Though no clear separation exists, there is a cluster of no plume detection at high  
344 SZA and low normalized radiance. This is a consistent and expected relationship, as SZA and surface  
345 reflectance are principal drivers of the quantity of light that is observed by the satellite, and therefore  
346 SNR of the observation.

347



348

349 **Figure 4.** CO<sub>2</sub> plume prediction using various atmospheric, retrieval, and bottom-up information.

350 Panel (a) shows the results of fitting a logistic regression classification model to the set of PRISMA

351 acquisitions where an analyst identified the presence or lack of a plume. Panel (b) shows the top two  
352 explanatory variables (SZA and normalized radiance) along with plume classification.

353

354 The logistic regression model performed better on the test data set than predictions made at  
355 random, though the prediction performance was still low. Missing from the model is sub-annually  
356 resolved information regarding operating status. For most of the power plants outside the U.S., we  
357 do not have information on daily operations of a power plant. In many cases of non-detects, we could  
358 simply be observing a power plant temporarily not in operation. Another possibility is that at the time  
359 of acquisition, some power plants were operating at reduced capacity, meaning that CO<sub>2</sub> emission  
360 rates were lower than those predicted by annual emission factors or activity data. If the true CO<sub>2</sub>  
361 emission rate was below the minimum detection limit (MDL) possible by the PRISMA satellite, then  
362 it would show as a non-detect. However, even if the emission were near or slightly above the  
363 PRISMA MDL, the probability of detection would still be low as slight variations in atmospheric  
364 properties, as seen in Figure 4, would then influence the ability to detection a CO<sub>2</sub> plume.

365

### 366 *3.2 Validation of PRISMA and OCO-3 emission rates against CEMS*

367 For each power plant where a CO<sub>2</sub> plume was identified, we quantify emissions using the  
368 IME approach described by Equations 5-7. In order to estimate the XCO<sub>2</sub> mass enhancement ( $\Delta\Omega$  in  
369 Equation 1), a local background must be quantified and subtracted from total XCO<sub>2</sub> retrievals across  
370 the scene. To do this, we apply a concentration threshold  $\beta$  to initiate the plume masking and  
371 segmentation process (described in Methods section). Once we have a plume mask, we apply another  
372 concentration threshold  $\gamma$  to the remaining XCO<sub>2</sub> pixels that exist outside of the plume. This value  $\gamma$   
373 represents the XCO<sub>2</sub> background that we use to calculate the XCO<sub>2</sub> enhancement that is used in the

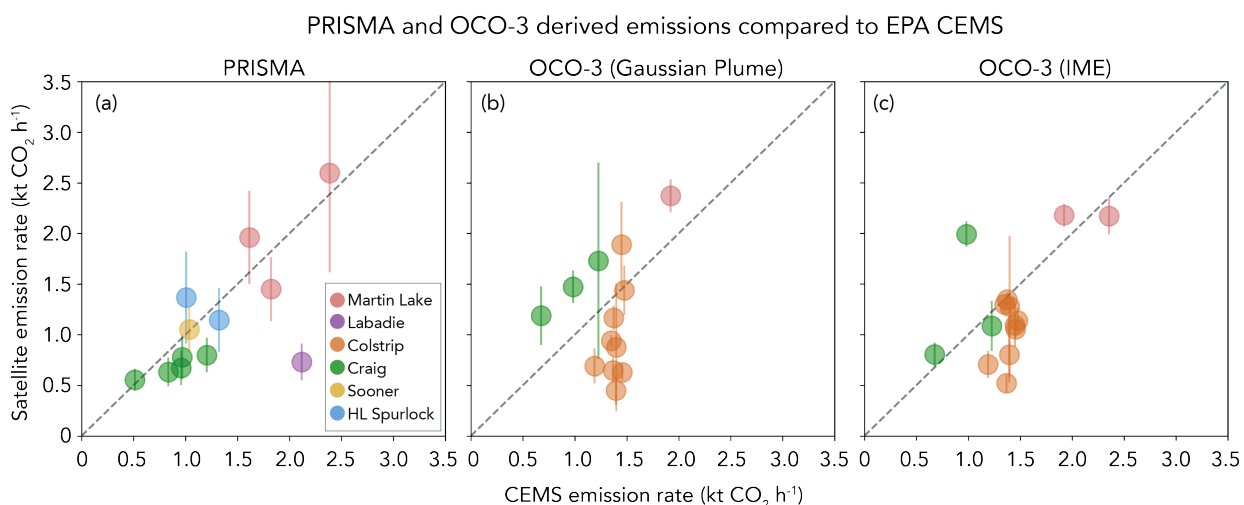
374 IME formulation of Equation 1. Thresholds  $\beta$  and  $\gamma$  largely influence the magnitude of the emission  
375 rate and are not known a priori. For global generalizability, we wish to estimate  $\beta$  and  $\gamma$  such that  
376 they do not vary across power plants, seasons, regions, etc. Therefore, we parameterize  $\beta$  and  $\gamma$  as  
377 percentiles under the assumption that the local contrast between enhanced CO<sub>2</sub> plume pixels and the  
378 background should be similar across PRISMA scenes.

379 To estimate values for  $\beta$  and  $\gamma$ , we compare EPA CEMS data for power plants in the U.S.  
380 with estimated emission rates from PRISMA. In total, we have 12 scenes in the U.S. with CEMS  
381 information that pertain to 5 power plants. We then optimize  $\beta$  and  $\gamma$  such that the output of an  
382 ordinary least squares regression produces a slope near unity. Figure 5a shows the results of this  
383 optimization which produces an optimal  $\beta$  percentile of 94% and a  $\gamma$  percentile of 62%. The results  
384 also show decent correlation between CEMS data and PRISMA-derived emission rates ( $R^2 = 0.43$ ).  
385 A single outlier at the Labadie power plant (imaged July 10, 2022) shows the largest discrepancy  
386 from CEMS data (69%), but the remaining plumes show average 27% relative difference from CEMS  
387 data. If we remove the one data point at Labadie, the  $R^2$  improves to 0.75. Though a limited sample  
388 size, between PRISMA and OCO-3, these scenes represent variability in solar geometries (20-40°  
389 SZA), surface reflectance (0.09-0.90 normalized radiance), and reported emission rates (0.51 – 2.39  
390 kt CO<sub>2</sub> h<sup>-1</sup>). Therefore, we use these optimal parameters and apply them to our global dataset of  
391 PRISMA detections. These emission rates are reported in Table 1. There are some instances when  
392 performing IME emission calculations using these thresholds and plume masking technique do not  
393 result in emission rates (e.g., the plume masking procedure produces a mask with no pixels). In these  
394 cases, we report a detection but not an emission quantification.

395 Figures 5b and 5c shows the comparison between OCO-3 and CEMS at some power plants  
396 that overlap with PRISMA observations (14 scenes total). OCO-3 Gaussian plume model emission

397 rates (Fig. 5b) have an improved correlation compared to PRISMA ( $R^2 = 0.51$ ), although with greater  
 398 bias (average 47% relative difference from CEMS). The OCO-3 IME estimates (Fig. 5c) have worse  
 399  $R^2$  (0.32) but a better RMSE (0.45 kt CO<sub>2</sub>/hr) compared to the Gaussian plume model estimates (0.84  
 400 kt CO<sub>2</sub>/hr), with 9 of the 14 cases being within 30% of the reported CEMS emission and an average  
 401 relative difference of 30% for all 14 cases. Additionally, the least squares fit for IME is closer to the  
 402 1-to-1 line than for the Gaussian plume model.

403



404

405 **Figure 5.** Comparison of emission rates in the U.S. between satellite-derived estimates and CEMS  
 406 information. Panel (a) shows a comparison between PRISMA derived emission rates and CEMS ( $R^2$   
 407 = 0.43), panel (b) shows a comparison between OCO-3 and CEMS using the Gaussian plume model  
 408 ( $R^2 = 0.51$ ), and panel (c) shows a comparison between OCO-3 and CEMS using IME ( $R^2 = 0.32$ ).

409

410 Unique sources of error for OCO-3 emission estimates include geolocation errors in the  
 411 XCO<sub>2</sub> product. These errors are typically less than 1 km, but can be up to 2 km (Taylor et al., 2023).  
 412 Errors of this magnitude, about the size of an OCO-3 footprint ( $\sim 2 \times 2$  km<sup>2</sup>), may mean that an entire

413 footprint is not included when estimating emissions using the Gaussian plume method, which  
414 assumes that the plume only extends downwind of the known source location. The Gaussian plume  
415 model is also susceptible to wind direction errors, and requires the plume to be Gaussian in shape,  
416 which is often not true. IME, while not suffering from wind direction or geolocation-induced errors,  
417 assumes that the entire plume is captured in a given SAM, which is sometimes not true and results in  
418 an underestimation of emissions. IME is also sensitive to errors in  $U_{eff}$  parameterization.

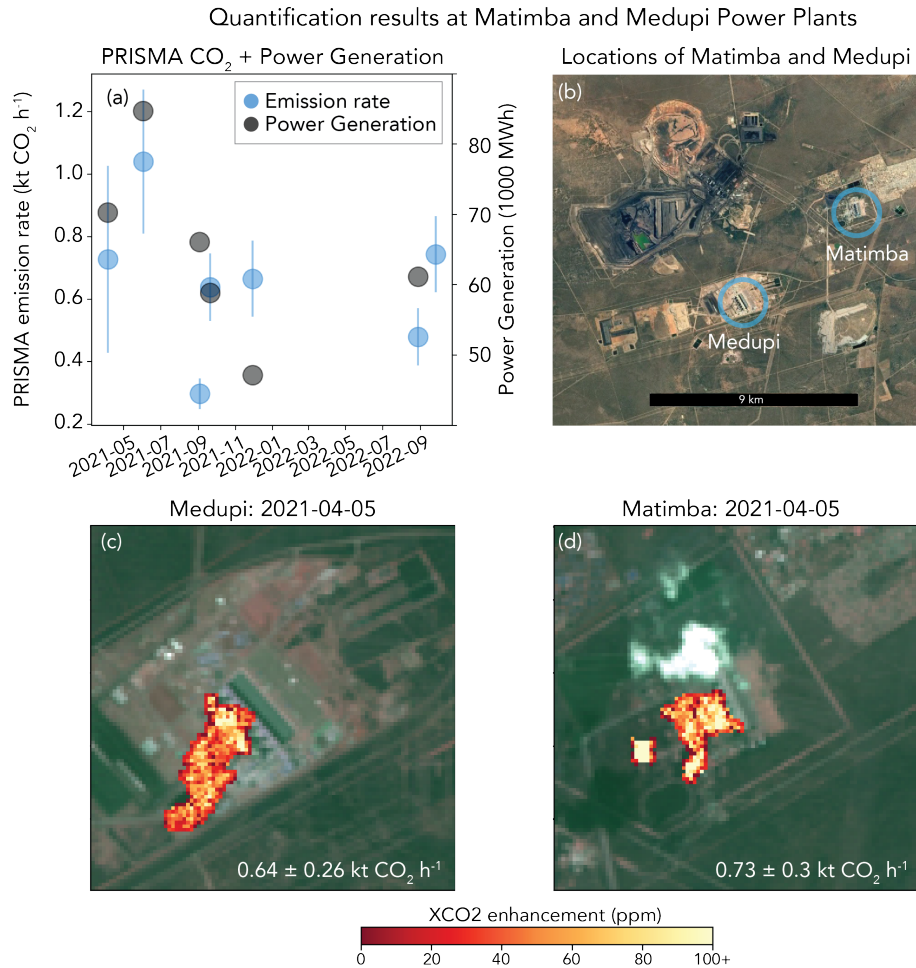
419

### 420 *3.3 Comparison and fusion of PRISMA and OCO*

421 Outside the U.S., PRISMA observed the Matimba power station in South Africa 11 times and  
422 quantified emission rates 7 times. Emissions from Matimba have previously been quantified and  
423 validated using OCO-2 (Hakkarainen et al., 2021). This station does not report hourly emission rates,  
424 but does report daily power generation (Eskom, 2023). Though not a direct comparison, we can use  
425 this information to check if the emission quantification approach we describe above captures some  
426 variability in activity at this power plant. Figure 6a shows the emission rates we quantified compared  
427 against reported power generation. We see rough agreement in variability – the high power  
428 generation reported between Apr to July 2021 (70000-85000 MWh) drop for subsequent dates  
429 (47000-66000 MWh) between Sep 2021 to Sep 2022, a drop which is also seen in the PRISMA-  
430 derived CO<sub>2</sub> emission rate. Across all observations, we estimate an emission rate range of 0.30-1.04  
431 kt CO<sub>2</sub> h<sup>-1</sup> (average 0.66 kt CO<sub>2</sub> h<sup>-1</sup>). This average emission rate is substantially lower than the  
432 average 2.50 kt CO<sub>2</sub> h<sup>-1</sup> emission rate estimated from OCO-2 and TROPOMI between 2018-2020,  
433 but within the range of emissions estimates directly quantified with OCO-2 (0.30-7.20 kt CO<sub>2</sub> h<sup>-1</sup>;  
434 Hakkarainen et al., 2021). However, this discrepancy could be result of (1) changes in activity or  
435 variability or (2) existence of other nearby emission sources. For changes in activity, during August

436 2020, the Matimba reported a large range of power generation (65000-94000 MWh) and emission  
437 estimates derived directly from OCO-2 were also highly variable (0.88-4.33 kt CO<sub>2</sub> h<sup>-1</sup>). Given that  
438 maximum power generation at the time of a PRISMA observation was 85000 MWh, some of the  
439 discrepancy in maximum CO<sub>2</sub> quantification between PRISMA and OCO-2 could be due to activity.

440         Nearby (7 km) the Matimba Power Station is the Medupi Power Plant (Figure 6b). Figure 6c  
441 show the Medupi CO<sub>2</sub> plume observed during the same PRISMA overpass on Apr 5, 2021. The  
442 PRISMA derived emission rate for Medupi is  $0.64 \pm 0.26$  kt CO<sub>2</sub> h<sup>-1</sup> and for Matimba is  $0.73 \pm 0.30$   
443 kt CO<sub>2</sub> h<sup>-1</sup>. Given the proximity of the two power plants, the higher derived emission rate reported  
444 for Matimba from previous studies could actually be a result of a net emission from these two  
445 facilities. The OCO-2 flight track is located tens of kilometers downwind from Matimba and Medupi,  
446 making a clear delineation between potentially co-emitted distinct emission plumes near impossible.  
447 If we sum emission rates from both Medupi and Matimba, we quantify a range of 0.89-1.73 kt CO<sub>2</sub>  
448 h<sup>-1</sup> ( $1.30 \pm 0.28$  kt CO<sub>2</sub> h<sup>-1</sup>), which is still lower, but closer to the average emissions quantified by  
449 OCO-2.



450

451 **Figure 6.** Emission rates and reported power generation at the Matimba and Medupi power plants in  
 452 South Africa. Panel (a) shows the CO<sub>2</sub> emission rates derived from PRISMA and the reported daily  
 453 power generation for the day of PRISMA overpass. Panel (b) shows the locations of the Medupi and  
 454 Matimba power plants (base imagery provided by Google Earth; © Google Earth 2023). Panels (c)  
 455 and (d) show plume imagery and emission rates for a PRISMA overpass on Apr 5, 2021.

456

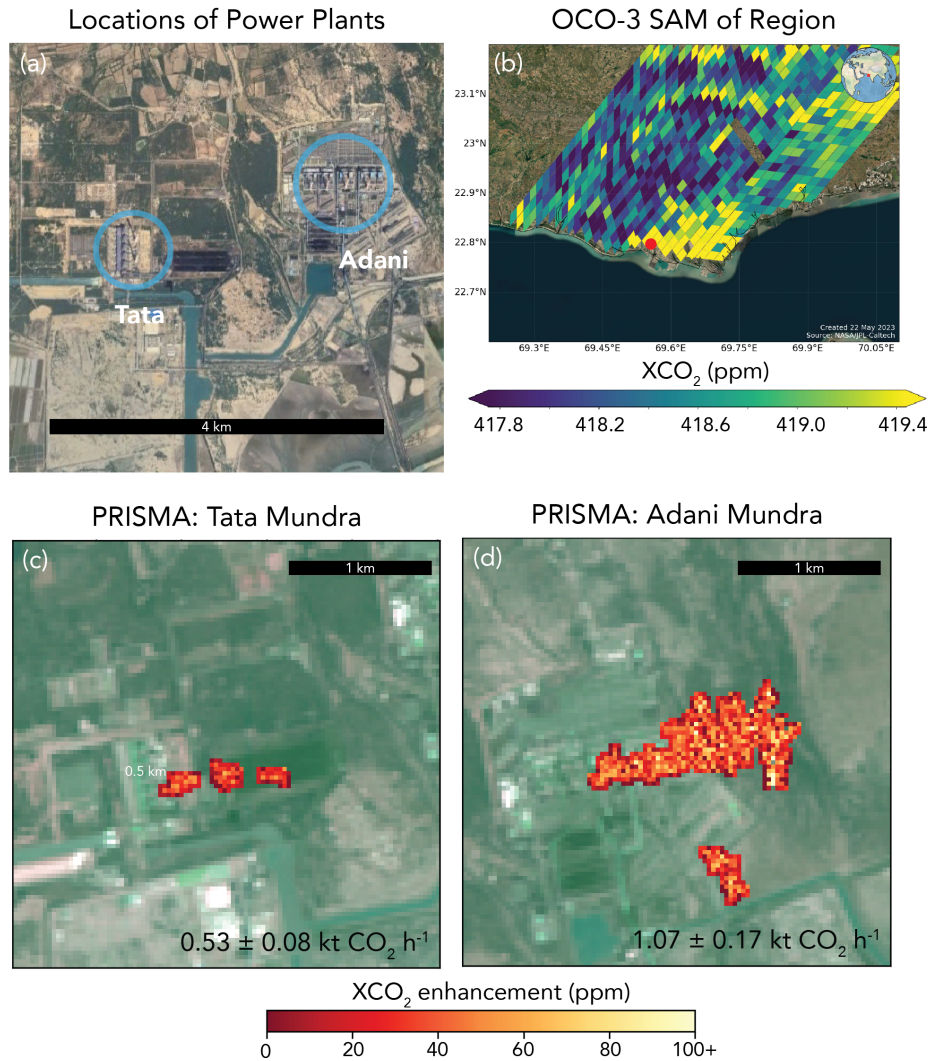
457 The ability to differentiate the contribution of unique point sources to a regional total is an  
 458 application made possible by joint observing of imaging spectrometers and atmospheric sounders.

459 Figure 7 shows observations that were made at the Tata Mundra Ultra Mega Power Plant and the



460 Adani Mundra Thermal Power Project: two power plants less than 3 km apart. Both OCO-3 and  
461 PRISMA imaged the power plants on Apr 9, 2022. Figure 7b shows the OCO-3 SAM (taken 04:41  
462 UTC) – large CO<sub>2</sub> enhancements appear along the coastline likely associated with emission from  
463 these power plants. PRISMA imaged the power plants less than two hours later (06:02 UTC) and  
464 detected CO<sub>2</sub> plumes at each facility (Figure 7b-c). The OCO-3 derived emission rate using Gaussian  
465 plume approaches is  $5.5 \pm 0.7$  kt CO<sub>2</sub> h<sup>-1</sup>, but the emission rate derived using the IME approach is  
466 much lower ( $3.0$  kt CO<sub>2</sub> h<sup>-1</sup>). For this case, the IME approach may be more appropriate as the shape  
467 of the OCO-3 plume (Figure 7b) is more diffuse in nature and does not visibly resemble a Gaussian  
468 structure. The PRISMA emission rate for the Adani plant is  $1.07 \pm 0.17$  kt CO<sub>2</sub> h<sup>-1</sup> and for the Tata  
469 Mundra plant is  $0.53 \pm 0.08$  kt CO<sub>2</sub> h<sup>-1</sup>. We can use this information to estimate that 67% of the net  
470 CO<sub>2</sub> emission came from Adani, and the remaining 33% came from the Tata plant. The combined  
471 emission rate ( $1.60 \pm 0.25$  kt CO<sub>2</sub> h<sup>-1</sup>) is lower than the OCO-3 IME emission rate. Like the Matimba  
472 power plant, some of this discrepancy may partially be explained by bias or uncertainty in retrievals,  
473 background, and wind information. Also, lower estimates of CO<sub>2</sub> emissions from PRISMA are  
474 consistent with the fact that PRISMA is only sensitive to emissions at two exhaust stacks, while the  
475 OCO-3 observation includes all CO<sub>2</sub> sources in the industrial area around Mundra. Continued  
476 validation of retrieved emission rates against ground standards (e.g., CEMS) will help better quantify  
477 bias and uncertainty. However, even with lingering uncertainty, the near simultaneous observations  
478 of OCO-3 and PRISMA can help us disentangle the relative contributions from each power plant.  
479

Near-simultaneous OCO-3 & PRISMA observations (2022-04-09)



480

481 **Figure 7.** Near-simultaneous observation of two power plants in Mundra, India on Apr 9, 2022. Panel  
482 (a) shows the locations of two power plants spaced less than 3 km apart: Tata Mundra and Adani  
483 Mundra Power Stations (base imagery provided by Google Earth; © Google Earth 2023). Panel (b)  
484 shows the OCO-3 SAM with a red dot showing the location of the power plants. Panel (c) and (d)  
485 show the PRISMA acquisition (less than 2 hours after OCO-3) over the two power plants with  
486 associated emission rates.

487

488 **Conclusion**

489 We observed a global set of power plants for two years between 2021-2022 with both  
490 PRISMA and OCO-3 to test the ability of these satellite platforms to do routine operational  
491 monitoring of CO<sub>2</sub> emissions. When PRISMA observations were of sufficient quality to perform  
492 XCO<sub>2</sub> retrievals, we detected CO<sub>2</sub> plumes nearly half of the time. We fit a logistic regression  
493 classification using plume detections and find that there is some relationship between SZA and  
494 surface reflectance that partially explains plume prediction; consistent given that these factors are  
495 major drivers of SNR. The remaining non-plume detections may be due to operational status of a  
496 power plant at the time of observation. We compared emission rates from both PRISMA and OCO-  
497 3 to power plants in the U.S. where we have access to hourly *in situ* CEMS emission information.  
498 We find significant correlation between satellite and *in situ* estimates, though some significant biases  
499 may exist for some of the observations for both PRISMA and OCO-3. Also, the quantity of CEMS  
500 observations was limited (~10 for each instrument), so robust calibration is not yet possible. Still,  
501 early results show that under the right conditions, satellites can provide reliable estimates of CO<sub>2</sub>  
502 emissions at discrete point source locations. This is consistent with the close agreement between  
503 airborne imaging spectrometer emissions and CEMS information (Cusworth et al., 2021).

504 Fusion of information from atmospheric sounders like OCO-3 and imaging spectrometers  
505 like PRISMA is valuable for cross-validation and source attribution. We see this particularly for our  
506 examples at the Matimba and Medupi power plants in South Africa and the Tata and Adani power  
507 plants in Mundra, India. In these cases, and particularly at Mundra where near-simultaneous  
508 PRISMA and OCO-3 observations were taken, OCO-2/3 provides a local, but coarse resolution  
509 emission constraint for a complex of facilities that emit large CO<sub>2</sub> quantities. PRISMA, with its 30  
510 m pixel resolution, then can help refine relative contributions of single emitters against the net

511 emission flux. More work is needed to refine cross-validation between instruments, but initial  
512 observation shows one avenue for data from multiple observing systems to be complementary  
513 aggregated and analyzed.

514 Even when combining information from both satellites, there is still too little sampling to  
515 constrain facility emissions within low uncertainties. Cusworth et al. (2021), using arguments from  
516 Hill and Nassar (2019), suggested that nearly 30 unbiased observations from a PRISMA-class  
517 instrument is needed per year at each power plant to reduce annual uncertainties below 14% (i.e.,  
518 reduce emission uncertainty from Non-Annex I countries below 1 Gt CO<sub>2</sub> per year). No power plant  
519 in this study met this minimum sampling requirement. However, there will be a significant increase  
520 in data volumes and observation performance of satellite remote sensing capabilities for CO<sub>2</sub>, from  
521 both recently launched and planned imaging spectrometers including EMIT (launched 2022; Thorpe  
522 et al., in revision); EnMAP (launched 2022; Guanter et al., 2015); Carbon Mapper/Tanager 1-2  
523 (Planned launch 2024; Duren et al., 2021), and atmospheric sounders including CO<sub>2</sub>M (Sierk et al.,  
524 2019). Improved observation of global power plants and emission quantification with robust error  
525 characterization will be vital to reduce global uncertainty of anthropogenic emissions from fossil fuel  
526 combustion sources.

527

#### 528 **Data Availability.**

529 The OCO-3 XCO<sub>2</sub> and other retrieval properties are publicly available at the NASA Goddard Earth  
530 Science Data and Information Services Center (GES-DISC). The full suite of retrieval products in  
531 the standard per-orbit format can be obtained at OCO Science Team et al., 2021,  
532 <https://doi.org/10.5067/D9S8Z0CHCADE>. The lightweight per-day format data (Lite files), which  
533 includes the bias corrected estimates of XCO<sub>2</sub>, can be obtained at OCO Science Team et al., 2022,

534 <https://doi.org/10.5067/970BCC4DHH24>. PRISMA data including radiance for each scene and  
535 XCO2 retrievals is available at <https://doi.org/10.5281/zenodo.8083596>.

536

537 **Acknowledgments.** This work was supported by the Orbiting Carbon Observatory Science Team.  
538 We thank the Italian Space Agency for the PRISMA satellite targets. Portions of this work were  
539 undertaken at the Jet Propulsion Laboratory, California Institute of Technology, under contract with  
540 NASA.

541

542 **Author Contributions.** DHC designed the study. DHC, AKA, RJ tasked and acquired PRISMA  
543 data. DHC performed PRISMA emission quantification and validation. RRN performed OCO-3  
544 quantification and validation. RN and JPM helped implement OCO-3 quantification algorithms. All  
545 authors provided feedback on results and the manuscript.

546

547

548 **Competing interests.** The authors declare no conflicts of interest.

549

## 550 **References**

551 Beirle, S., Borger, C., Dörner, S., Eskes, H., Kumar, V., de Laat, A. and Wagner, T., 2021. Catalog  
552 of NO<sub>x</sub> emissions from point sources as derived from the divergence of the NO<sub>2</sub> flux for  
553 TROPOMI. *Earth System Science Data*, 13(6), pp.2995-3012. DOI [https://doi.org/10.5194/essd-13-](https://doi.org/10.5194/essd-13-2995-2021)  
554 2995-2021

555

556 Bell, B., Hersbach, H., Berrisford, P., Dahlgren, P., Horányi, A., Sabater, M., et al.

557 (2020). ERA5 hourly data on pressure levels from 1950 to 1978 (preliminary  
558 version). Copernic. Clim. Change Serv. (C3S) Clim. Data Store (CDS). AvailableAt:  
559 [https://cds.climate.copernicus-climate.eu/cdsapp#!/dataset/reanalysis-era5-  
561 pressure-levels-preliminary-back-extension?tab=overview](https://cds.climate.copernicus-climate.eu/cdsapp#!/dataset/reanalysis-era5-<br/>560 pressure-levels-preliminary-back-extension?tab=overview).

562 Bell, E., O'Dell, C.W., Taylor, T.E., Merrelli, A., Nelson, R.R., Kiel, M., Eldering, A., Rosenberg,  
563 R. and Fisher, B., 2023. Exploring bias in the OCO-3 snapshot area mapping mode via geometry,  
564 surface, and aerosol effects. *Atmospheric Measurement Techniques*, 16(1), pp.109-133. DOI  
565 <https://doi.org/10.5194/amt-16-109-2023>

566

567 Brunner, D., Kuhlmann, G., Henne, S., Koene, E., Kern, B., Wolff, S., Voigt, C., Jöckel, P.,  
568 Kiemle, C., Roiger, A. and Fiehn, A., 2023. Evaluation of simulated CO2 power plant plumes from  
569 six high-resolution atmospheric transport models. *Atmospheric Chemistry and Physics*, 23(4),  
570 pp.2699-2728. DOI <https://doi.org/10.5194/acp-23-2699-2023>

571

572 Crippa, M., Guizzardi, D., Banja, M., Solazzo, E., Muntean, M., Schaaf, E., Pagani, F., Monforti-  
573 Ferrario, F., Olivier, J., Quadrelli, R., Riquez Martin, A., Taghavi-Moharamli, P., Grassi, G.,  
574 Rossi, S., Jacome Felix Oom, D., Branco, A., San-Miguel-Ayanz, J. and Vignati, E., CO2  
575 emissions of all world countries - 2022 Report, EUR 31182 EN, Publications Office of the  
576 European Union, Luxembourg, 2022, [doi:10.2760/730164](https://doi.org/10.2760/730164), JRC130363

577 Crisp, D., Fisher, B.M., O'Dell, C., Frankenberg, C., Basilio, R., Bösch, H., Brown, L.R., Castano,  
578 R., Connor, B., Deutscher, N.M. and Eldering, A., 2012. The ACOS CO2 retrieval algorithm—part

579 II: global XCO<sub>2</sub> data characterization. *Atmospheric Measurement Techniques*, 5(4), pp.687-707.  
580 DOI <https://doi.org/10.5194/amt-5-687-2012>  
581  
582 Cusworth, D.H., Duren, R.M., Thorpe, A.K., Eastwood, M.L., Green, R.O., Dennison, P.E.,  
583 Frankenberg, C., Heckler, J.W., Asner, G.P. and Miller, C.E., 2021. Quantifying global power plant  
584 carbon dioxide emissions with imaging spectroscopy. *AGU Advances*, 2(2), p.e2020AV000350.  
585 DOI <https://doi.org/10.1029/2020AV000350>  
586  
587 Dougherty, E.R., 1992. An introduction to morphological image processing. In *SPIE*. Optical  
588 Engineering Press.  
589  
590 Duren, R., Cusworth, D., Ayasse, A., Herner, J., Thorpe, A., Falk, M., Heckler, J., Guido, J.,  
591 Giuliano, P., Chapman, J. and Green, R., 2021, December. Carbon Mapper: on-orbit performance  
592 predictions and airborne prototyping. In *AGU Fall Meeting Abstracts* (Vol. 2021, pp. A53F-05).  
593  
594 Eldering, A., Taylor, T.E., O'Dell, C.W. and Pavlick, R., 2019. The OCO-3 mission: measurement  
595 objectives and expected performance based on 1 year of simulated data. *Atmospheric Measurement*  
596 *Techniques*, 12(4), pp.2341-2370. DOI <https://doi.org/10.5194/amt-12-2341-2019>  
597  
598 Fan, R.E., Chang, K.W., Hsieh, C.J., Wang, X.R. and Lin, C.J., 2008. LIBLINEAR: A library for  
599 large linear classification. *the Journal of machine Learning research*, 9, pp.1871-1874. DOI  
600 <https://doi.org/10.5555/1390681.1442794>  
601

602 Gelaro, R., McCarty, W., Suárez, M.J., Todling, R., Molod, A., Takacs, L., Randles, C.A.,  
603 Darmenov, A., Bosilovich, M.G., Reichle, R. and Wargan, K., 2017. The modern-era retrospective  
604 analysis for research and applications, version 2 (MERRA-2). *Journal of climate*, 30(14), pp.5419-  
605 5454. <https://doi.org/10.1175/JCLI-D-16-0758.1>

606  
607 GEM, Global Energy Monitor's Global Coal Plant Tracker, URL  
608 <https://globalenergymonitor.org/projects/global-coal-plant-tracker/tracker/>, last accessed May 24,  
609 2023

610  
611 Guan, D., Liu, Z., Geng, Y., Lindner, S. and Hubacek, K., 2012. The gigatonne gap in China's  
612 carbon dioxide inventories. *Nature Climate Change*, 2(9), pp.672-675. DOI  
613 <https://doi.org/10.1038/nclimate1560>

614  
615 Guanter, L., Kaufmann, H., Segl, K., Foerster, S., Rogass, C., Chabrillat, S., Kuester, T., Hollstein,  
616 A., Rossner, G., Chlebek, C. and Straif, C., 2015. The EnMAP spaceborne imaging spectroscopy  
617 mission for earth observation. *Remote Sensing*, 7(7), pp.8830-8857. DOI  
618 <https://doi.org/10.3390/rs70708830>

619  
620 Guo, W., Shi, Y., Liu, Y. and Su, M., 2023. CO2 emissions retrieval from coal-fired power plants  
621 based on OCO-2/3 satellite observations and a Gaussian plume model. *Journal of Cleaner*  
622 *Production*, 397, p.136525. DOI <https://doi.org/10.1016/j.jclepro.2023.136525>

623



624 Hakkarainen, J., Szeląg, M.E., Ialongo, I., Retscher, C., Oda, T. and Crisp, D., 2021. Analyzing  
625 nitrogen oxides to carbon dioxide emission ratios from space: A case study of Matimba Power  
626 Station in South Africa. *Atmospheric Environment: X*, 10, p.100110. DOI  
627 <https://doi.org/10.1016/j.aeaoa.2021.100110>  
628

629 Hill, T. and Nassar, R., 2019. Pixel size and revisit rate requirements for monitoring power plant  
630 CO<sub>2</sub> emissions from space. *Remote Sensing*, 11(13), p.1608. DOI  
631 <https://doi.org/10.3390/rs11131608>  
632

633 Hong, C., Zhang, Q., He, K., Guan, D., Li, M., Liu, F. and Zheng, B., 2017. Variations of China's  
634 emission estimates: response to uncertainties in energy statistics. *Atmospheric Chemistry and  
635 Physics*, 17(2), pp.1227-1239. DOI <https://doi.org/10.5194/acp-17-1227-2017>  
636

637 IPCC, 2021: *Climate Change 2021: The Physical Science Basis. Contribution of Working Group I  
638 to the Sixth Assessment Report of the Intergovernmental Panel on Climate Change*[Masson-  
639 Delmotte, V., P. Zhai, A. Pirani, S.L. Connors, C. Péan, S. Berger, N. Caud, Y. Chen, L. Goldfarb,  
640 M.I. Gomis, M. Huang, K. Leitzell, E. Lonnoy, J.B.R. Matthews, T.K. Maycock, T. Waterfield, O.  
641 Yelekçi, R. Yu, and B. Zhou (eds.)]. Cambridge University Press, Cambridge, United Kingdom and  
642 New York, NY, USA, In press, doi:[10.1017/9781009157896](https://doi.org/10.1017/9781009157896).  
643

644 J. Muñoz-Sabater, Dutra, E., Agustí-Panareda, A., Albergel, C., Arduini, G., Balsamo, G.,  
645 Boussetta, S., Choulga, M., Harrigan, S., Hersbach, H., Martens, B., Miralles, D. G., Piles, M.,  
646 Rodríguez-Fernández, N. J., Zsoter, E., Buontempo, C., and Thépaut, J.-N.: ERA5-Land: A state-

647 of-the-art global reanalysis dataset for land applications, *Earth Syst. Sci. Data*,13, 4349–4383,  
648 2021. <https://doi.org/10.5194/essd-13-4349-2021>.  
649  
650 Kochanov, R.V., Gordon, I.E., Rothman, L.S., Weisło, P., Hill, C. and Wilzewski, J.S., 2016.  
651 HITRAN Application Programming Interface (HAPI): A comprehensive approach to working with  
652 spectroscopic data. *Journal of Quantitative Spectroscopy and Radiative Transfer*, 177, pp.15-30.  
653 DOI <https://doi.org/10.1016/j.jqsrt.2016.03.005>  
654  
655 Lin, X., van der A, R., de Laat, J., Eskes, H., Chevallier, F., Ciais, P., Deng, Z., Geng, Y., Song, X.,  
656 Ni, X. and Huo, D., 2023. Monitoring and quantifying CO<sub>2</sub> emissions of isolated power plants  
657 from space. *EGUsphere*, pp.1-20. DOI <https://doi.org/10.5194/egusphere-2022-1490>  
658  
659 Loizzo, R., Guarini, R., Longo, F., Scopa, T., Formaro, R., Facchinetti, C. and Varacalli, G., 2018,  
660 July. PRISMA: The Italian hyperspectral mission. In *IGARSS 2018-2018 IEEE International*  
661 *Geoscience and Remote Sensing Symposium* (pp. 175-178). IEEE. DOI [https://doi.org/](https://doi.org/10.1109/IGARSS.2018.8518512)  
662 [10.1109/IGARSS.2018.8518512](https://doi.org/10.1109/IGARSS.2018.8518512)  
663  
664 Nassar, R., Hill, T.G., McLinden, C.A., Wunch, D., Jones, D.B. and Crisp, D., 2017. Quantifying  
665 CO<sub>2</sub> emissions from individual power plants from space. *Geophysical Research Letters*, 44(19),  
666 pp.10-045. DOI <https://doi.org/10.1002/2017GL074702>  
667  
668 Nassar, R., Mastrogiacomo, J.P., Bateman-Hemphill, W., McCracken, C., MacDonald, C.G., Hill,  
669 T., O'Dell, C.W., Kiel, M. and Crisp, D., 2021. Advances in quantifying power plant CO<sub>2</sub>

670 emissions with OCO-2. *Remote Sensing of Environment*, 264, p.112579. DOI  
671 <https://doi.org/10.1016/j.rse.2021.112579>  
672  
673 Nassar, R., Moeini, O., Mastrogiacomo, J.P., O'Dell, C.W., Nelson, R.R., Kiel, M., Chatterjee, A.,  
674 Eldering, A. and Crisp, D., 2022. Tracking CO2 emission reductions from space: A case study at  
675 Europe's largest fossil fuel power plant. *Frontiers in Remote Sensing*, 3, p.98. DOI  
676 <https://doi.org/10.3389/frsen.2022.1028240>  
677  
678 O'Dell, C.W., Connor, B., Bösch, H., O'Brien, D., Frankenberg, C., Castano, R., Christi, M.,  
679 Eldering, D., Fisher, B., Gunson, M. and McDuffie, J., 2012. The ACOS CO 2 retrieval algorithm–  
680 Part 1: Description and validation against synthetic observations. *Atmospheric Measurement*  
681 *Techniques*, 5(1), pp.99-121. DOI <https://doi.org/10.5194/amt-5-99-2012>  
682  
683 O'Dell, C.W., Eldering, A., Wennberg, P.O., Crisp, D., Gunson, M.R., Fisher, B., Frankenberg, C.,  
684 Kiel, M., Lindqvist, H., Mandrake, L. and Merrelli, A., 2018. Improved retrievals of carbon dioxide  
685 from Orbiting Carbon Observatory-2 with the version 8 ACOS algorithm. *Atmospheric*  
686 *Measurement Techniques*, 11(12), pp.6539-6576. DOI <https://doi.org/10.5194/amt-11-6539-2018>  
687  
688 Rodgers, C.D., 2000. *Inverse methods for atmospheric sounding: theory and practice* (Vol. 2).  
689 World scientific.  
690  
691 Reuter, M., Buchwitz, M., Schneising, O., Krautwurst, S., O'Dell, C.W., Richter, A., Bovensmann,  
692 H. and Burrows, J.P., 2019. Towards monitoring localized CO2 emissions from space: co-located

693 regional CO<sub>2</sub> and NO<sub>2</sub> enhancements observed by the OCO-2 and S5P satellites. *Atmospheric*  
694 *Chemistry and Physics*, 19(14), pp.9371-9383. DOI <https://doi.org/10.5194/acp-19-9371-2019>  
695

696 Sierk, B., Bézy, J.L., Löscher, A. and Meijer, Y., 2019, July. The European CO<sub>2</sub> Monitoring  
697 Mission: observing anthropogenic greenhouse gas emissions from space. In *International*  
698 *Conference on Space Optics—ICSO 2018* (Vol. 11180, pp. 237-250). SPIE. DOI [https://doi.org/](https://doi.org/10.1117/12.2535941)  
699 [10.1117/12.2535941](https://doi.org/10.1117/12.2535941)  
700

701 Taylor, T.E., O'Dell, C.W., Baker, D., Bruegge, C., Chang, A., Chapsky, L., Chatterjee, A., Cheng,  
702 C., Chevallier, F., Crisp, D. and Dang, L., 2023. Evaluating the consistency between OCO-2 and  
703 OCO-3 XCO<sub>2</sub> estimates derived from the NASA ACOS version 10 retrieval  
704 algorithm. *Atmospheric Measurement Techniques Discussions*, 2023, pp.1-61. DOI  
705 <https://doi.org/10.5194/amt-16-3173-2023>  
706

707 Thorpe, A.K., Frankenberg, C., Thompson, D.R., Duren, R.M., Aubrey, A.D., Bue, B.D., Green,  
708 R.O., Gerilowski, K., Krings, T., Borchardt, J. and Kort, E.A., 2017. Airborne DOAS retrievals of  
709 methane, carbon dioxide, and water vapor concentrations at high spatial resolution: application to  
710 AVIRIS-NG. *Atmospheric Measurement Techniques*, 10(10), pp.3833-3850. DOI  
711 <https://doi.org/10.5194/amt-10-3833-2017>  
712

713 Van Geffen, J., Boersma, K.F., Eskes, H., Sneep, M., Ter Linden, M., Zara, M. and Veeffkind, J.P.,  
714 2020. S5P TROPOMI NO<sub>2</sub> slant column retrieval: Method, stability, uncertainties and comparisons

715 with OMI. *Atmospheric Measurement Techniques*, 13(3), pp.1315-1335. DOI

716 <https://doi.org/10.5194/amt-13-1315-2020>

717

718 Varon, D.J., Jacob, D.J., McKeever, J., Jervis, D., Durak, B.O., Xia, Y. and Huang, Y., 2018.

719 Quantifying methane point sources from fine-scale satellite observations of atmospheric methane

720 plumes. *Atmospheric Measurement Techniques*, 11(10), pp.5673-5686. DOI

721 <https://doi.org/10.5194/amt-11-5673-2018>